Nanoscale



PAPER View Article Online
View Journal | View Issue



Cite this: Nanoscale, 2022, 14, 127

Reversible assembly of silica nanoparticles at water-hydrocarbon interfaces controlled by SDS surfactant†

Sohaib Mohammed, o a Ivan Kuzmenko and Greeshma Gadikota ** **

Achieving reversible and tunable assembly of silica nanoparticles at liquid-liquid interfaces is vital for a wide range of scientific and technological applications including sustainable subsurface energy applications, catalysis, drug delivery and material synthesis. In this study, we report the mechanisms controlling the assembly of silica nanoparticles (dia. 50 nm and 100 nm) at water-heptane and water-toluene interfaces using sodium dodecyl sulfate (SDS) surfactant with concentrations ranging from 0.001-0.1 wt% using operando ultrasmall/small-angle X-ray scattering, cryogenic scanning electron microscopy imaging and classical molecular dynamics simulations. The results show that the assembly of silica nanoparticles at water-hydrocarbon interfaces can be tuned by controlling the concentrations of SDS. Silica nanoparticles are found to: (a) dominate the interfaces in the absence of interfacial SDS molecules, (b) coexist with SDS at the interfaces at low surfactant concentration of 0.001 wt% and (c) migrate toward the aqueous phase at a high SDS concentration of 0.1 wt%. Energetic analyses suggest that the van der Waals and electrostatic interactions between silica nanoparticles and SDS surfactants increase with SDS concentration. However, the favorable van der Waals and electrostatic interactions between the silica nanoparticles and toluene or heptane decrease with increasing SDS concentration. As a result, the silica nanoparticles migrate away from the water-hydrocarbon interface and towards bulk water at higher SDS concentrations. These calibrated investigations reveal the mechanistic basis for tuning silica nanoparticle assembly at complex interfaces

Received 14th October 2021, Accepted 28th November 2021 DOI: 10.1039/d1nr06807e

rsc.li/nanoscale

1. Introduction

Achieving tunable controls on the dispersion behavior of silica nanoparticles in water and hydrocarbon-bearing environments is crucial for probing their migration, precipitation and scaling behavior for emerging sustainable subsurface energy applications including CO₂ storage in hydrocarbon-bearing reservoirs. The changes in the porosity and permeability in subsurface geologic environments resulting from the migration, aggregation and precipitation of fine siliceous matter remain largely unexplored in the context of harnessing reservoirs for fluid storage and recovery. While the adsorption of surfactants on mineral or rock surfaces is known to be influenced by nanoparticles, ^{1,2} the mechanisms underlying surfactant-induced assembly of silica nanoparticles at water-hydrocarbon interfaces remain less explored. The ability to tune

interfacial tension for coalescing and stabilizing oil-in-water emulsions is crucial for energy efficient water-hydrocarbon separations. Despite the presence of suspended silica nanoparticles in natural aqueous environments,³ their influence on stabilizing oil-in-water emulsions has not been studied.

Furthermore, advances in the use of engineered silica nanoparticles to architect new matter for applications related to delivery,6,7 catalysis,4,5 synthesis,8,9 drug materials separation, 10,11 sensors, 12 adsorption, 13 enhanced oil recovery14 and food processing15 motivate us to develop mechanistic insights into the assembly of silica nanoparticles at complex fluidic interfaces. For example, Pickering emulsions have been used as polymerization vessels for preparing hollow microcapsules and composites capsules.16 These materials are widely used in food, pharmaceutical and cosmetic products. Advancing fundamental insights into the interfacial behavior and the energetic interactions underlying the organization of silica nanoparticles and surfactants at complex interfaces is crucial for synthesizing novel materials. With this context, the following questions are addressed in this study: (i) What is the influence of surfactant concentrations on the organization or displacement of silica nanoparticles at water-hydrocarbon

^aSchool of Civil and Environmental Engineering, Cornell University, Ithaca, New York 14853, USA. E-mail: gg464@cornell.edu; Tel: +1 607-255-4796

 $[^]b$ Advanced Photon Source, Argonne National Laboratory, Lemont, Illinois 60439, USA † Electronic supplementary information (ESI) available. See DOI: 10.1039/d1nr06807e

interfaces? (ii) How does the interfacial behavior of surfactants and silica nanoparticles evolve with the size of nanoparticles? (iii) What are the energetic interactions underlying the organization or displacement of silica nanoparticles away from water-hydrocarbon interfaces?

Prior experimental and computational studies utilized various techniques, including Pendant drop tensiometer and molecular dynamics simulations^{17–22} to probe the interfacial behavior of surfactants and nanoparticles at various water-hydrocarbon interfaces. While some studies concluded that the synergetic interactions of nanoparticles and surfactants on the interface enhance emulsion stability,^{22–27} others reported that the surfactant concentrations higher than the critical micelle concentration (CMC) leads to the displacement of the nanoparticles from the interface.^{28,29} Although it is poorly understood, the mechanism governing the displacement of nanoparticles from the interface is related to the interfacial tension of the associated emulsion and the contact angle between the nanoparticles and the liquid phases.¹⁷

The energy required to displace a nanoparticle from the interface can be quantified as $E = \pi r^2 \gamma_{OW} (1 \pm \cos \varphi)^2$ where r is the radius of the nanoparticle, $\gamma_{\rm OW}$ is the interfacial tension of the oil-water emulsion, and φ is the contact angle of the adsorbed nanoparticles at the interface.³⁰ The extent to which the nanoparticles adsorb at the interface depends on the wettability of these nanoparticles. Nanoparticles with highly hydrophilic or hydrophobic surfaces tend to disperse in water or hydrocarbon phases, respectively. According to the equation above, the maximum energy required to displace a nanoparticle from the interface is at a contact angle of 90°. The synergetic interactions of surfactants and nanoparticles on the interface can alter the wetting properties of the assembled nanoparticles and eventually enhance or inhibit the assembly of nanoparticles on the interface. Vashisth and co-workers²⁹ showed that adding high surfactant concentrations can completely disrupt the assembly of nanoparticles from the interface because the presence of the surfactant at the water-oil interface is energetically favored compared to nanoparticles. This displacement was also attributed to the influence of the added surfactants on the nanoparticle's contact angle at the interface, 31,32 the extent of nanoparticles flocculation, 33,34 the dynamics of nanoparticles at the interface³⁵ and the competitive assembly of surfactant molecules at the interface.³⁶ Resolving the synergetic effects of surfactant and nanoparticles enables us to tune the self-assembly behavior of nanoparticles at water-hydrocarbon interfaces in addition to the ability to control the interfacial properties of the associated emulsion including the coalescence of small drops into larger drops that facilitate the separation of water and oil phases.

In this study, we introduce an experimental and computational approach to elucidate the interfacial behavior underlying the co-existence of silica nanoparticles with diameters of 50 nm and 100 nm and sodium dodecyl sulfate (SDS) concentrations ranging from 0.001–0.1% at water–heptane and water–toluene interfaces. Ultrasmall- and Small-Angle X-Ray Scattering (USAXS/SAXS) measurements, Cryogenic Scanning

Electron Microscopy (Cryo-SEM) imaging, and Molecular Dynamics (MD) simulations are harnessed to probe the coexistence of hydrophilic silica nanoparticles and SDS molecules on the interfaces and their influence on the interfacial properties of the studied emulsions. The interfacial behavior of the silica nanoparticles is investigated at SDS concentrations of 0.001, 0.01 and 0.1 wt%. The experiments and simulations are performed at 1 bar and 298 K. This experimental and simulation approach enables us to develop fundamental insights into the structure, dynamics and morphology of nanoparticles and surfactant assembled at water–hydrocarbon interfaces across spatial and temporal scales.

2. Methodology

2.1. Sample preparation

Silica nanoparticles with diameters of 50 nm and 100 nm dispersed in Milli-Q water with a concentration of 10 mg ml⁻¹ (1 wt%) purchased from nanoComposix, Inc. are used. The sizes and the dispersion states of the nanoparticles are confirmed by measuring the USAXS/SAXS intensities of the solutions bearing nanoparticles prior to the preparation of the emulsions. The average size of the well dispersed nanoparticles is confirmed to be 51.35 \pm 3.15 nm and 101.35 \pm 4.17 nm using USAXS/SAXS measurements.³⁷ The suspensions of 50 nm and 100 nm nanoparticles have a pH of 9.7 and 7.4, respectively. ζ potential of the 50 nm and 100 nm nanoparticles suspensions are -51 mV and -59 mV, respectively. SDS surfactant are purchased from Sigma-Aldrich and used without further treatment. SDS powder is dissolved in high purity (99.9%) heptane and toluene solvents to produce solutions with SDS concentrations of 0.001 wt%, 0.01 wt%, and 0.1 wt%. The SDS solutions are stirred at 800 rpm under 298 K for 2 hours to ensure complete dissolution of the added surfactant. The water-heptane and water-toluene interfaces are prepared by injecting 50 µl of the nanoparticles' suspensions followed by 50 µl of the SDS solutions in a glass vial with a diameter of about 1 mm (see Fig. 1(a)). The emulsions were left undisturbed at 298 K for 24 hours prior to characterization.

2.2. Ultra-small/small angle X-ray scattering (USAXS/SAXS) measurements

The assembly of silica nanoparticles and surfactant at the water–hydrocarbon interfaces are determined using Ultra-Small/Small Angle X-Ray Scattering (USAXS/SAXS) measurements. These measurements are performed by detecting the scattered X-ray beam from the interfaces of the water–hydrocarbon emulsions on a 2D detector (see Fig. 1(a)). The experiments are conducted at sector 9-ID-C in the Advanced Photon Source (APS) at Argonne National Laboratory. The total X-ray flux is 10¹³ photon/mm²s. The energy of the incident X-ray beam during the measurement is 21.0 keV that corresponds to a wavelength of 0.589 Å. The scattered USAXS data are collected using a Bonse-Hart camera and the scattered SAXS data are acquired using a pinhole camera on a Pilatus

Nanoscale Paper

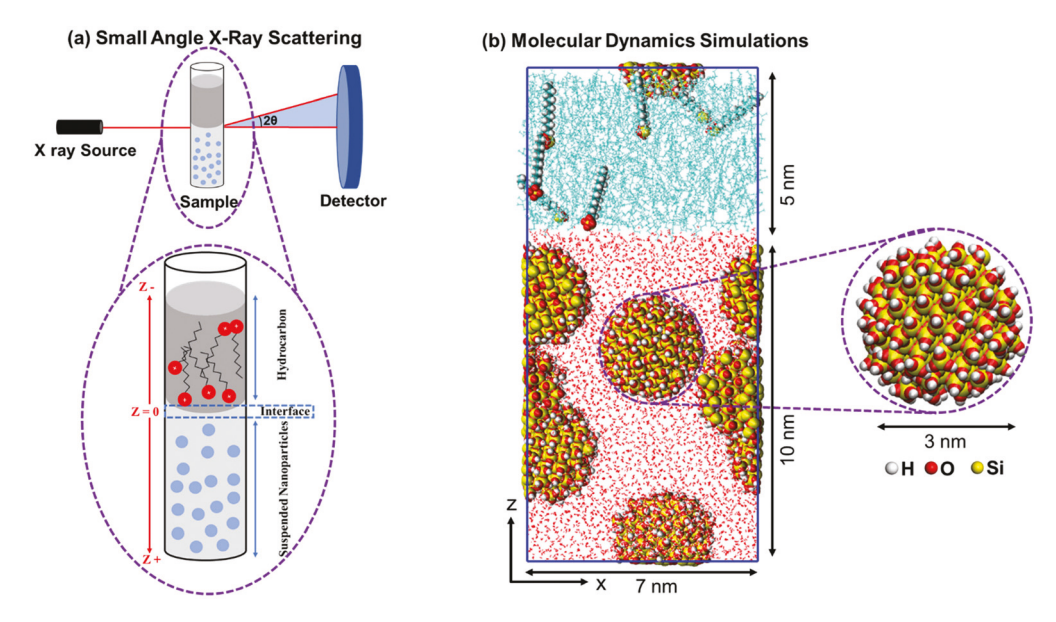


Fig. 1 Schematic representation of the experimental setup of ultra-small/small-angle X-ray scattering (USAXS/SAXS) measurements of silica nanoparticles and sodium dodecyl sulfate surfactant at water-heptane and water-toluene interfaces is shown in panel (a). Snapshot of the simulated initial configuration of the suspended silica nanoparticles in the water phase and the suspended SDS molecules in the hydrocarbon phase is shown in panel (b). The atoms of silica nanoparticles (see the color coding for the atoms) and SDS molecules are drawn using VDW drawing method while water and hydrocarbons molecules are drawn using Lines method implemented in VMD visualization software.

100 K detector (Dectris Ltd, Baden Switzerland). The data acquisition times for the USAXS and SAXS measurements are 90 and 5 s, respectively. The 2D data are reduced and converted to 1D curves using the Nika (SAXS)40 and Irena (USAXS)⁴¹ macros implemented in Igor software. The background scattering from the interfaces of water-heptane and water-toluene interfaces free of surfactants and nanoparticles are collected and subtracted from the scattering data. The wavevector (Q) values (where $Q = (4\pi/\lambda) \sin \theta$, λ is the X-ray wavelength, and θ is one half of the scattering angle) and sample-to-detector distances (and geometry) are calibrated using silver behenate. Additional information about the X-ray scattering measurements is included in a prior publication by Mohammed and co-workers.37

2.3. Cryogenic scanning electron microscopy (Cryo-SEM)

Cryo-SEM imaging is performed using the FEI Strata 400S DualBeam instrument at the Cornell Center for Materials Research (CCMR) for high-resolution and high-contrast imaging. The prepared emulsions are frozen using liquid nitrogen to avoid changes in the interfacial structure of the nanoparticles and surfactants. The freezing time of the studied emulsions is in the order of milliseconds. Different regions at the water-heptane and water-toluene interfaces and in the bulk water phase are imaged to visualize the morphology of nanoparticles at various SDS concentrations.

2.4. Molecular dynamics simulations

Silica nanoparticle with a diameter of 3 nm is cleaved from a well-studied and validated β-cristobalite unit cell. The size of

the simulated nanoparticles is chosen for three main reasons: (a) the ease of modifying the surface chemistry of these nanoparticles to reflect the density of hydroxyl (OH) groups on the surface of the silica nanoparticles used in the experiment, (b) using 3 nm sized nanoparticles allows us to use a concentration of 10 mg ml⁻¹ (5 nanoparticles) in reasonably large simulation cells and (c) using 3 nm sized silica nanoparticles enables us to conduct the simulations for reasonably sufficient simulation time (50 ns) to reach equilibrated states and draw reliable conclusions. Further, simulating larger sized nanoparticles requires adopting other simulation techniques such as coarse-grained molecular dynamics (GCMD) and dissipative particles dynamics (DPD) in which the atomic scale description of molecules is not considered. For example, Yu and Zhou⁴² utilized CGMD to understand the curvature effect of silica nanoparticles with diameters of 2 to 10 nm on the adsorption of lysozyme enzyme. Although the size of silica nanoparticles used in the simulation is smaller than the nanoparticles used in the experiments, the interfacial behavior and trends in the energetic interactions can be accurately predicted.

The nonbridging surface oxygens on the nanoparticle's surface are functionalized with OH groups with a surface density of about 7.3 OH nm⁻². The rationale behind choosing this level of hydroxylation is driven by the chemistry of the nanoparticles used in the experiments which are dominated by silanol groups (Si-OH) on the surface and the typical density of OH groups on the silica surfaces used in previous studies. 43-45 Further, our reactive molecular dynamics simulations (ReaxFF) shows that nonbridging oxygens on the

surface of 3 nm sized silica nanoparticles undergo continuous hydroxylation when dissolved in 1 g cm⁻³ of water at 298 K and 1 bar (see Fig. S1 and S2†).

Five silica nanoparticles are randomly distributed in a 7 nm × 7 nm × 10 nm cell with a concentration of 1 wt% to match the experimental concentration of the silica nanoparticles suspensions. The simulation cell is extended in the z-direction by 5 nm and SDS-heptane and SDS-toluene mixtures are added with surfactant concentrations of 0 wt%, 0.001 wt%, 0.01 wt%, and 0.1 wt% (see Fig. 1(b)). The dimensions of the initial simulation cells are 7 nm \times 7 nm \times 15 nm in x, y and z directions, respectively. Periodic boundary conditions are used in the x, yand z directions.

Silica nanoparticles and water molecules are modeled using parameters from CLAYFF⁴⁶ and TIP4P,⁴⁷ respectively, while heptane, toluene and SDS molecules are modeled using the OPLS/AA forcefield 48,49 (see the forcefield parameters in Table S1†). The combination of OPLS/AA and CLAYFF forcefields have been used extensively in investigating the interactions of hydrocarbons and surfactants with silica surfaces. 50-52 50 000 steps of energy minimization using "steepest descent" method are performed on the initial configurations to decrease their high energy and remove the inappropriate geometries. The minimized configurations underwent semi-isotropic compression in z-direction, the direction normal to the interface for 50 ns using the constant number of molecules, constant pressure, constant interfacial area, and constant temperature (NPAT) ensemble. The simulations are performed at 1 bar and 298 K to be consistent with the experimental conditions. Nose-Hoover thermostat^{53,54} with a relaxation time of 1 ps and Parrinello-Rahman barostat⁵⁵ are used to maintain the required temperature and pressure. The equation of motion is integrated using the leapfrog algorithm with a time step of 1 fs. The short-range interactions are calculated within a cutoff of 1.4 nm, while the long-range electrostatic interactions are treated using Particle Mesh Ewald (PME). 56 The nonbonded van der Waals and electrostatic interactions are modeled using 12-6 Lennard-Jones and coulombic models, respectively. The bonded interactions account for bonds stretching, angles bending and dihedrals, except for silica nanoparticles where only OH bond stretching are accounted for. All the simulations are conducted using GROningen Machine for Chemical Simulations (GROMACS 2018) simulation package.⁵⁷

Results and discussion 3.

Assembly of nanoparticles and SDS on the interfaces

The assembly of silica nanoparticles and SDS molecules on water-heptane and water-toluene interfaces is evident from the USAXS/SAXS intensity curves (see Fig. 2). At 0 wt% SDS, the scattering curves suggest that water-heptane and watertoluene interfaces are dominated by 50 nm and 100 nm silica nanoparticles as the intensities shows a scattering pattern that corresponds to that of spherical nanoparticles. The assembly

behavior of silica nanoparticles with comparable sizes at water-heptane and water-toluene interfaces under similar conditions are evident from prior experimental and computational studies. 37,58 The scattering behavior from the interfacial silica nanoparticles is observed in the presence of 0.001 wt% SDS concentrations, suggesting the coexistence of nanoparticles and surfactant on water-heptane and water-toluene interfaces. Interestingly, as SDS concentrations increases to 0.01 wt%, the scattering curve from water-heptane interface indicates the dominance of silica nanoparticles, while the detected intensity from water-toluene interfaces suggests that SDS molecules occupy the interfacial region and displace the nanoparticles toward the aqueous phase. These results suggest that the higher interfacial energy of water-heptane systems drives an enhanced assembly of silica nanoparticles.

As 0.1 wt% SDS is added to the system, the water-heptane and water-toluene interfaces are completely occupied by SDS molecules and no scattering from nanoparticles was observed, suggesting that the interfacial nanoparticles are completely displaced from the interfaces and emerged in the water phase. The competitive assembly of silica nanoparticles and SDS molecules on water-hydrocarbon interfaces is consistent with prior experimental work showing that the small quantities of surfactant stabilized nanoparticle emulsions.^{29,59}

To determine the size distribution and the number of interfacial silica nanoparticles at water-heptane and water-toluene interfaces, we modeled the USAXS/SAXS curves that represent the scattering behavior of silica nanoparticles and surfactant at these interfaces. Quantitative analyses on the nanoparticles' dominated interfaces are performed by modeling the structure factor S(Q) and the form factor P(Q) of the intensity curves on the Q scale. The intensity I(Q) scattered from identical spherical nanoparticles can be expressed as the product of S(Q) and P(Q) such that:⁶⁰

$$I(\overrightarrow{Q}) = S(\overrightarrow{Q})P(\overrightarrow{Q})$$
 (1)

The size distribution and the number of interfacial silica nanoparticles at water-heptane and water-toluene interfaces (Fig. 3) are obtained from fitting P(Q) at the high Q regions. At 0 wt% SDS, the number of 50 nm and 100 nm nanoparticles assembled at water-toluene surfaces is higher compared to water-heptane interfaces. The number of 50 nm and 100 nm silica nanoparticles at water-heptane and water-toluene interfaces decreased substantially as the SDS concentration increased to 0.001 wt%, indicating that the added SDS molecules preferentially occupy the interfacial area and thus reduce the available area for the nanoparticles to adsorb on the interface. It is interesting to note that the number of interfacial silica nanoparticles at water-heptane interface remains similar when the concentrations of surfactants are 0.001 wt% and 0.01 wt% irrespective of the size of the nanoparticles (Fig. 3(a) and (c)). In contrast, the number of silica nanoparticles at the water-toluene interface dropped to zero on increasing the concentration of surfactants to 0.01 wt% and 0.1 wt% (Fig. 3(b) and (d)). These observations agree with the findings of Nanoscale **Paper**

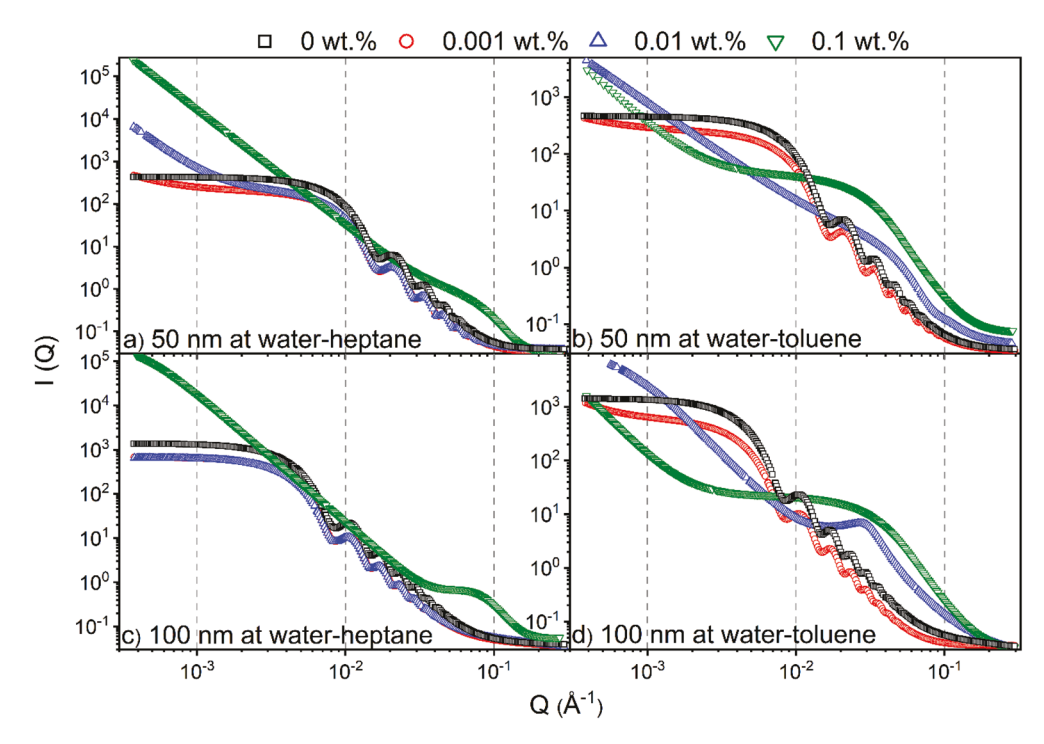


Fig. 2 Combined USAXS/SAXS scattering curves from water-heptane and water-toluene interfaces in the presence of (a) 50 nm nanoparticles on water-heptane, (b) 50 nm nanoparticles on water-toluene, (c) 100 nm nanoparticles on water-heptane and (d) 100 nm nanoparticles on watertoluene interfaces as a function of the SDS concentrations.

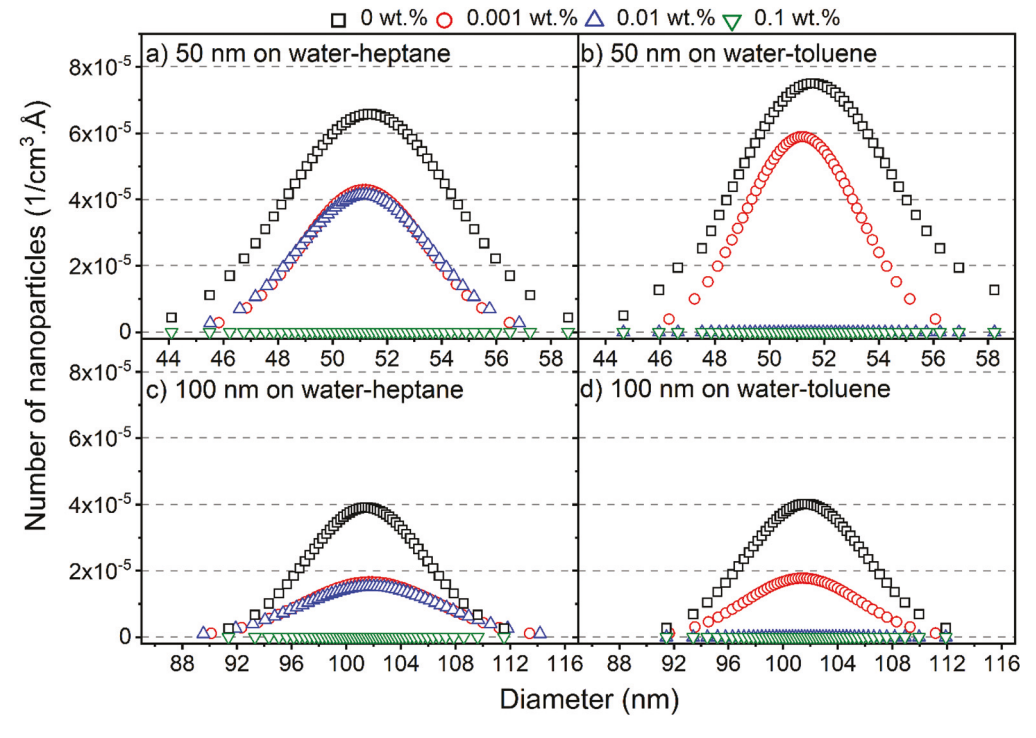


Fig. 3 Number of (a) 50 nm nanoparticles at water-heptane, (b) 50 nm nanoparticles at water-toluene, (c) 100 nm nanoparticles at water-heptane and (d) 100 nm nanoparticles at water-toluene interfaces as a function of SDS concentrations. The x-axis represents the size distribution of the interfacial silica nanoparticles. These data are governed from modeling the USAXS/SAXS scattering curves.

Vashisth and co-workers that interfacial surfactants displace the adsorbed nanoparticles after accounting for the difference in the sizes of nanoparticles.²⁹

The observations noted from Fig. 3 are consistent with the scattering data shown in Fig. 2. The scattering pattern from water-heptane and water-toluene interfaces at high SDS concentrations (i.e., 0.1 wt% at water-heptane and \geq 0.01 wt% at water-toluene) suggests the absence of silica nanoparticles at these interfaces and the dominance of surfactant assemblies (see Fig. 2). At 0.1 wt% SDS, the scattering curves from the water-heptane interfacial regions showed peaks at about 0.05 Å⁻¹ indicating scattering from self-assembled surfactant molecules. The scattering from self-assembled surfactant at water-toluene are noticed at 0.01 wt% and at 0.1 wt% SDS concentrations, whereas peaks are detected at about 0.031 Å⁻¹ and 0.026 Å⁻¹, respectively. The locations of the peaks in waterheptane and water-toluene interfaces show the dependence of the formed assembles sizes and morphologies on the interfacial properties of the corresponding emulsions. Porod analysis of the interfacial surfactants on water-heptane and water-toluene interfaces are performed at high Q region to investigate the morphology of the self-assembled SDS molecules (see Fig. 2). The power law slope values of the scattering intensity curves on water-heptane interfaces in the presence of 0.1 wt% are 2.4 and 2.3 for emulsions with 50 nm and 100 nm silica nanoparticles, respectively. These values indicate the formation of 2D disk-like morphologies by the interfacial surfactants. However, SDS molecules at the interfaces of watertoluene forms both 2D disk-like (Q^{-2}) and 1D rod-like (Q^{-1}) morphologies. The formation of surfactant ensembles on water-hydrocarbon interfaces are evident from prior experimental and computational studies. 61-64 Czajka and Armes 61 concluded that the presence of SDS surfactants results in the formation of spherical latex emulsions based on SAXS measurements. Shi and Guo⁶⁴ performed MD simulations on the effect of SDS molecular structure on its aggregation morphology at water-trichloroethylene interfaces. The results indicated that the surfactants form a continuous monolayer at the interface as the interfacial coverage increases.

The morphology of the self-assembled silica nanoparticles and SDS ensembles are further analyzed by calculating the power law slope in the USAXS (low Q) region (see Fig. 4). The morphology of self-assembled nanoparticles and SDS molecules change significantly with the SDS concentration. The low power law slope (< 1) in the absence (0 wt%) and presence of low SDS concentrations (0.001 wt%) indicate that the interfacial nanoparticles and SDS molecules are well dispersed at the interfaces. As the SDS concentration increases, the power law slope values increase substantially, implying the emergence of SDS aggregates with varying morphologies. A power law slope of < 3 indicates the formation of surface fractals. 65,66 Further, the displaced silica nanoparticles to the bulk water are well dispersed with no indication of self-assembly as the power low slope is < 1 in the USAXS region (see Fig. S3†).

The displacement of interfacial nanoparticles from waterheptane and water-toluene interfaces are confirmed by cryo-

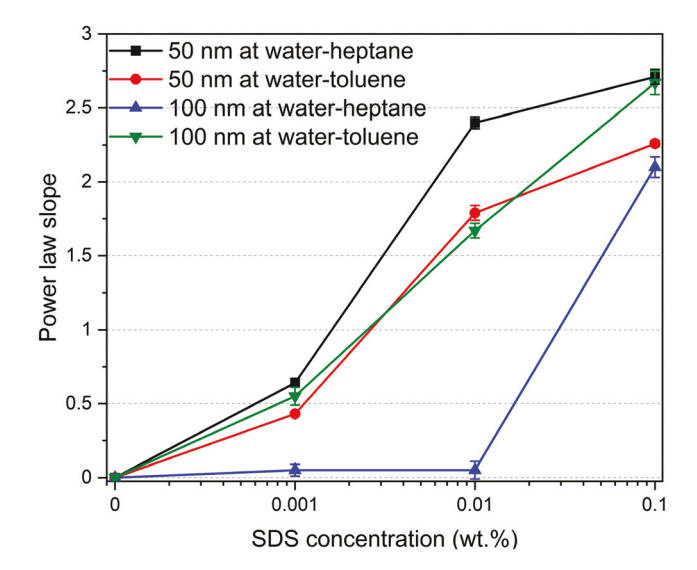


Fig. 4 Power law slope of the scattering curves in the ultrasmall angle X-ray scattering region of water-heptane and water-toluene emulsions with 50 nm and 100 nm silica nanoparticles as a function of SDS concentrations.

SEM imaging (see Fig. 5). At low SDS concentrations of 0.001 wt%, the nanoparticles are abundant in the interfacial region of water-heptane and water-toluene emulsions. The nanoparticles are mostly found as individual nanoparticles with minor traces as aggregates on water-heptane and watertoluene interfaces (see Fig. 5(a) and (c)). However, the number of interfacial nanoparticles on water-heptane and watertoluene interfaces were significantly reduced as the SDS concentration increased to 0.1 wt%. Only traces of nanoparticles are observed at the interfaces due to the displacement into the aqueous phase by the interfacial SDS assembles. The cryo-SEM data agrees with the observation of USAXS/SAXS scattering measurements (Fig. 2).

Additional insights into the assembly of silica nanoparticles and SDS molecules on water-heptane and water-toluene interfaces are obtained from the density profiles governed by MD simulations (Fig. 6). The density profiles are averaged over the last 10 ns of the simulation time and calculated along the axis normal to the interface (z-axis). Water and hydrocarbons formed two separated phases, while the silica nanoparticles and SDS molecules are dispersed in the water and hydrocarbon phases, respectively, with favorable assembly at the interfaces (Fig. 6(a) and (b)). The initially dispersed nanoparticles in the water phase migrated and assembled on the interfaces to extents that differ with the concentration of SDS molecules. SDS density profiles showed peaks at waterheptane and water-toluene interfaces, indicating preferential assembly at water-hydrocarbon interfaces compared to the dispersion in bulk hydrocarbons. Higher peaks in SDS profiles are observed on water-toluene interfaces compared to waterheptane interfaces.

Interestingly, the density profiles of silica nanoparticles at water-heptane interfaces showed a systematic shift toward the

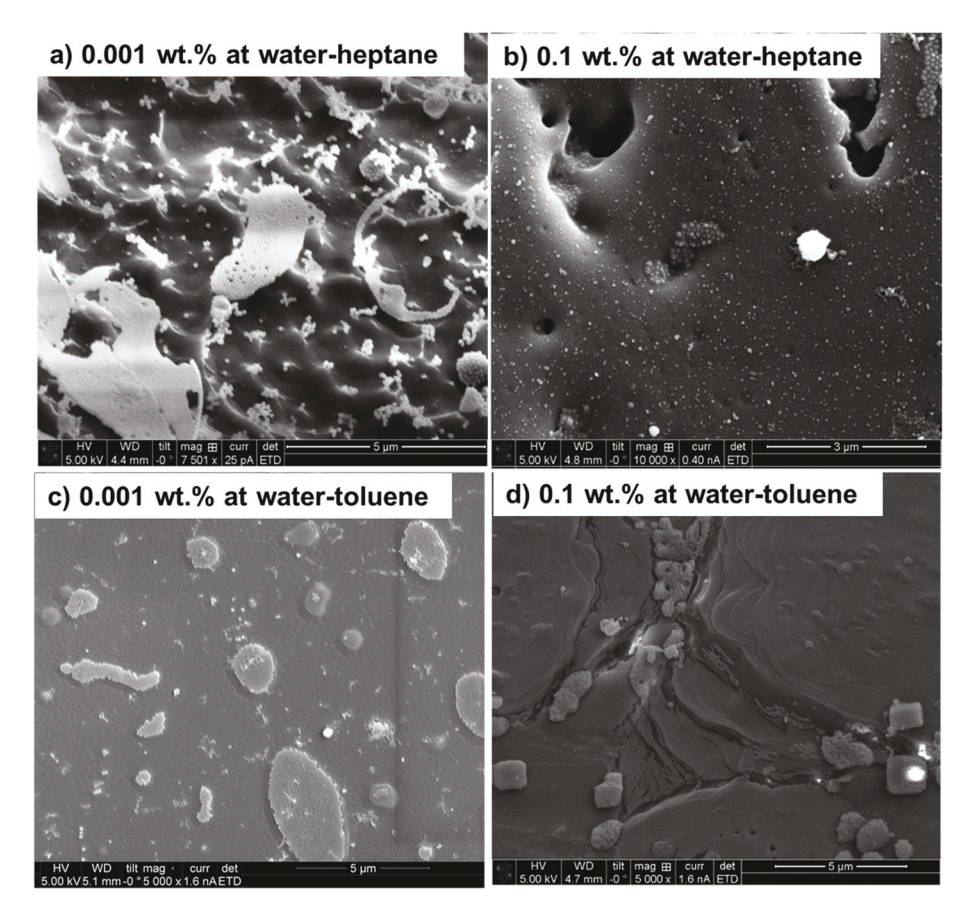


Fig. 5 Cryogenic scanning electron microscopy images of water-heptane and water-toluene interfaces in the presence of 0.001 wt% and 0.1 wt% SDS concentrations. The images are taken from systems containing 100 nm silica nanoparticles.

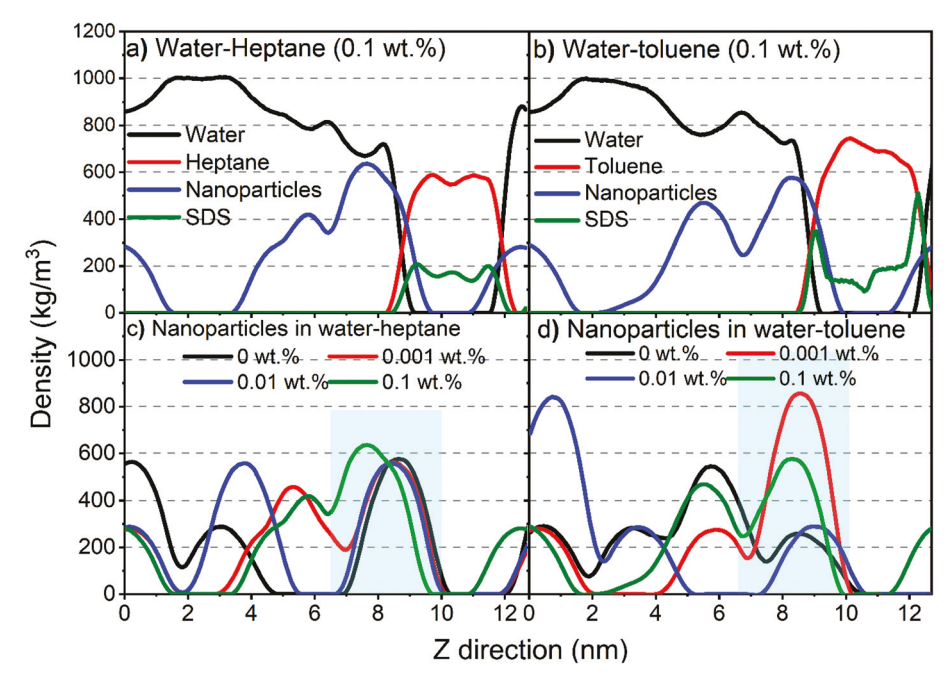


Fig. 6 The density profiles along the axis normal to the interface (z-axis) of (a) water-heptane system constituents in the presence of 0.1 wt% SDS, (b) water-toluene system constituents in the presence of 0.1 wt% SDS, (c) nanoparticles in water-heptane system as a function of SDS concentrations and (d) nanoparticles in water-toluene as a function of SDS concentrations. The density profiles are averaged over the last 10 ns of the simulation time.

water phase as the SDS concentrations increase in the system (Fig. 6(c)). The nanoparticles' density peaks at water-heptane interfaces are shifted from 8.7 nm to 7.6 nm as the SDS concentration increased from 0 wt% to 0.1 wt%, respectively. Similarly, the density peaks of nanoparticles at water-toluene are shifted from 8.5 nm to 8.3 nm as the SDS concentrations increased from 0 wt% to 0.1 wt%, respectively. The shift toward the aqueous phase suggests that the assembled SDS molecules on the interfaces displace the assembled nanoparticles away from the interface. This observation is consistent with the USAXS/SAXS intensities (Fig. 2 and 3) and agrees with previous studies.29

The displacement of nanoparticles from the interface is also evident from the density of water molecules around the surface of nanoparticles. These densities are quantified by calculating the radial distribution function (g(r)) of oxygen atoms in water molecules from the hydroxyl groups (-OH) on the surface of silica nanoparticles as a reference atom (see Fig. 7). The peaks represent the first coordination shells and second coordination shells of the oxygen in the water molecule around silica -OH groups. The density of the first and second coordination shells increased systematically with the increase in SDS concentrations. The denser water shells stem from the exposure of nanoparticle surface to water molecules that cover the nanoparticle as it is displaced from the interface and emerges into the aqueous phase to solvate the surfaces of nanoparticles and reduce its surface free energy.

3.2. Interfacial properties

The influence of SDS surfactants on the assembly of silica nanoparticles and the resulting impact on the interfacial pro-

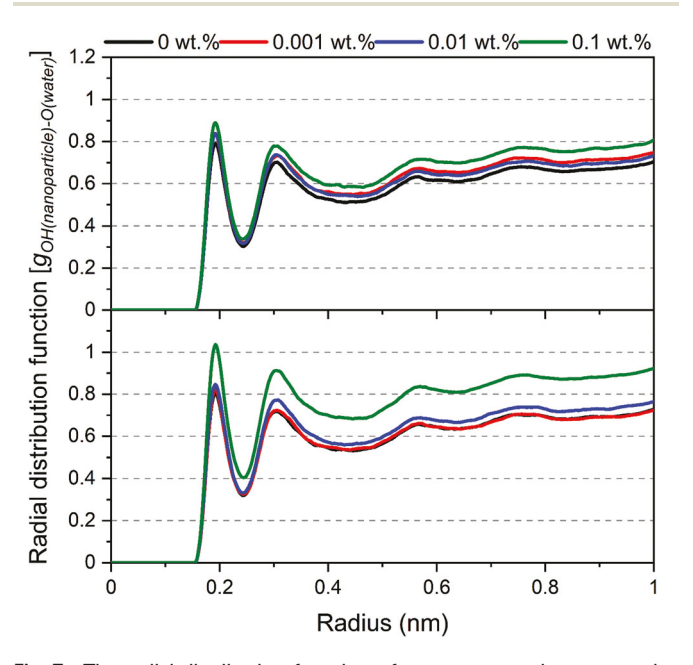


Fig. 7 The radial distribution function of oxygen atoms in water molecules from -OH groups on the silica nanoparticles surfaces as a function of SDS concentrations. The radial distribution functions are averaged over the last 10 ns of the simulation time.

perties of water-heptane and water-toluene emulsions is probed from the MD simulation trajectories. Water-heptane and water-toluene formed two distinct phases with average densities of about 994, 658 and 862 kg m⁻³ for water, heptane, and toluene phases, respectively (see Fig. 6), which is in excellent agreement with the experimental bulk and emulsion densities at the conditions of 1 bar and 298 K.67,68 The influence of silica nanoparticles and SDS surfactants on the interfacial properties is quantified by calculating the interfacial tensions of the studied emulsions (Fig. 8) as follow: 69,70

$$\gamma_{\text{WH}} = \frac{1}{n} \left(P_{zz} - \frac{P_{xx} + P_{yy}}{2} \right) L_z \tag{2}$$

In this expression, γ_{WH} is the interfacial tension of waterheptane and water-toluene mixtures, *n* is the number of interfaces in the simulation cell, P_{ii} is the pressure (where i = x, yand z directions) and L_z is the equilibrium cell length in the direction normal to the interface (z direction).

The calculated interfacial tensions of water-heptane and water–toluene at 1 bar and 298 K are 51.8 mN m^{-1} and 36.4 mN m⁻¹, respectively, which are consistent with prior experimental and simulation results.67,71 Introducing silica nanoparticles to the interface resulted in a 4.7% and 9.4% reduction in the interfacial tension of water-heptane and water-toluene mixtures, respectively. Increases in the SDS concentrations to 0.01 wt% resulted in a slight reduction in the interfacial tension of both emulsions due to the addition of limited quantities of surfactant molecules that accumulate at the water-hydrocarbon interfaces. A substantial reduction in the interfacial tensions of both emulsions is observed on adding 0.1 wt% of SDS to the systems. The interfacial tension of water-heptane and water-toluene decreased to 24.3 and

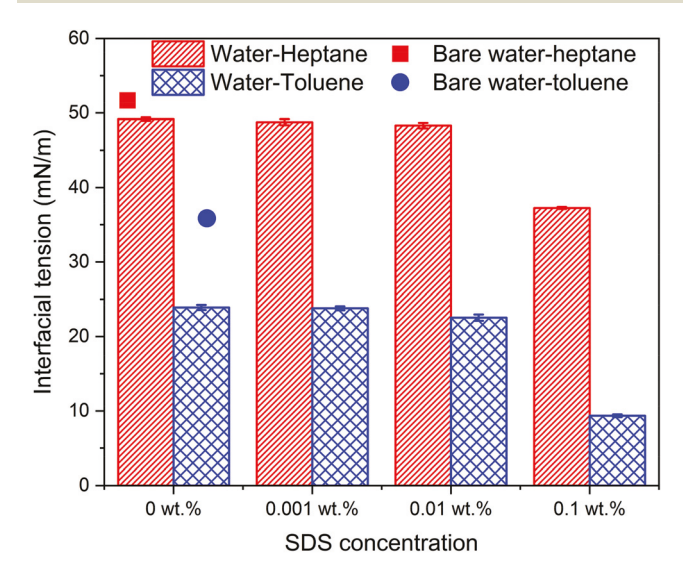


Fig. 8 The interfacial tension of water-heptane and water-toluene emulsions in the absence and presence of silica nanoparticles as a function of SDS concentrations. The interfacial tensions are averaged over the last 10 ns of the simulation time. The error bars represent the standard deviation from the mean value of three different simulations.

Nanoscale Paper

9.1 mN m⁻¹, respectively. These results suggest that high concentrations of SDS are more effective in stabilizing the emulsion of interest compared to hydrophilic silica nanoparticles. The simulations and experiments reveal that the stabilization of waterhydrocarbon emulsions in the presence of high concentrations of SDS surfactants is accompanied by limiting the assembly of silica nanoparticles at water-hydrocarbon interfaces.

The mechanism by which silica nanoparticles and SDS molecules reduce the interfacial tension of water-heptane and water-toluene emulsions involves the assembly and dispersion of these nanoparticles and surfactant at the interfaces (see Fig. 9). Silica nanoparticles form a cluster of five nanoparticles at water-heptane and water-toluene in the absence of SDS molecules. Interestingly, the aggregation number of the nanoparticles decreases systematically as the SDS concentration

increases (Fig. 9A and B) due to the preferential assembly of the SDS molecules at the interfacial region (Fig. 9C and D). Thus, the reduction in the interfacial tensions is driven by three scenarios (Fig. 9E): (a) the presence of nanoparticles at the interface results in slight reduction in the interfacial tension, (b) the coexistence of nanoparticles and surfactant at the interface results in a greater reduction in the interfacial tension compared to the first scenario, and (c) the excess SDS molecules at the interfaces of water-heptane and watertoluene reduces the interfacial tension significantly.

3.3. Energetics associated with the assembly of silica nanoparticles and SDS surfactant

The intermolecular interactions of silica nanoparticles with water and hydrocarbons are probed to elucidate the energetic

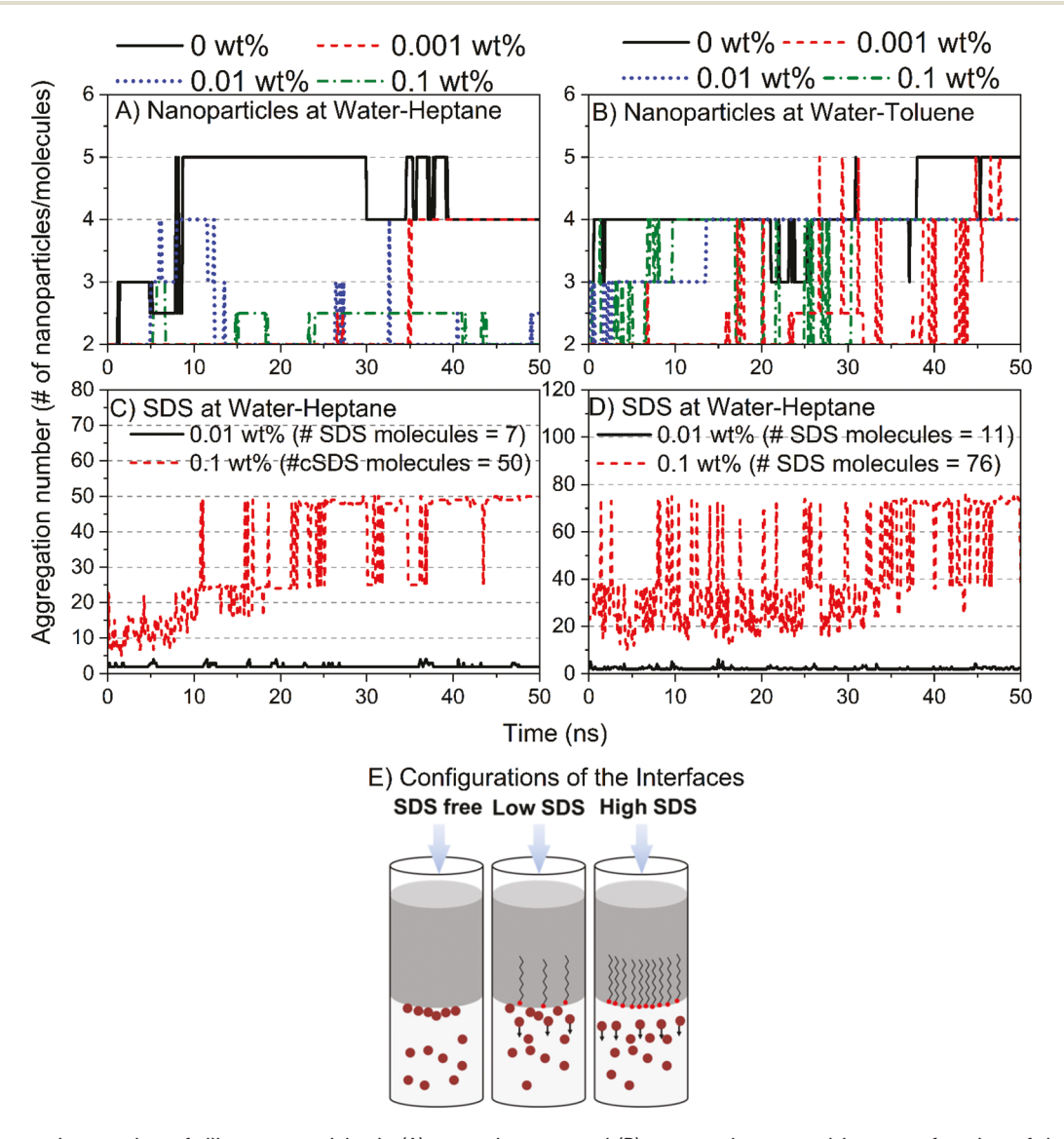


Fig. 9 The aggregation number of silica nanoparticles in (A) water-heptane and (B) water-toluene emulsions as a function of the SDS concentration. The assembly of SDS molecules at (C) water-heptane and (D) water-toluene interfaces are characterized by calculating the average aggregation number of SDS molecules at a concentration of 0.01 and 0.1 wt%. (E) Schematics show the interfacial configurations of silica nanoparticles and SDS surfactant at water-hydrocarbons interfaces at different SDS concentrations.

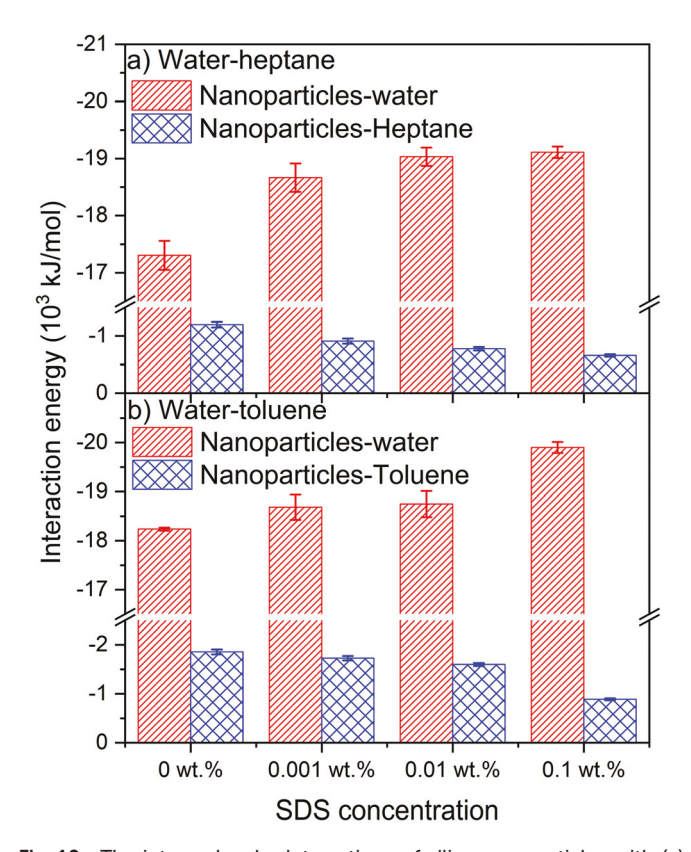


Fig. 10 The intermolecular interactions of silica nanoparticles with (a) water and heptane in water-heptane emulsion and (b) water and toluene in water-toluene emulsion as a function of the SDS concentrations. The intermolecular interactions are averaged over the last 10 ns of the simulation time. The error bars represent the standard deviation from the mean value of three different simulations.

Table 1 The number of water oxygens in the first coordination shell of hydroxyl group on the silica nanoparticles surface as a function of SDS concentrations. The data are averaged over the last 10 ns of the simulation time and the error bars represent the standard deviation from the mean value of three different simulations

SDS concentration (wt%)	Water-heptane	Water-toluene
0	0.43 ± 0.01	0.43 ± 0.02
0.001	0.45 ± 0.04	0.44 ± 0.01
0.01	0.47 ± 0.02	0.47 ± 0.03
0.1	0.48 ± 0.02	$\textbf{0.54} \pm \textbf{0.01}$

basis underlying their observed assembly as a function of SDS concentration (see Fig. 10). The van der Waals and electrostatic interactions averaged over the last 10 ns of the simulation constitute the intermolecular interactions of interest. The intermolecular interactions of the nanoparticles with water molecules are higher than the interactions of nanoparticles with heptane and toluene due to the hydrophilic nature of silica nanoparticles that drives the largest portion of the interfacial nanoparticle surface to be covered by water molecules.

Interestingly, the interactions of nanoparticles with water in water-heptane and water-toluene systems increase systematically with the SDS concentrations. The increase in nanoparticles-water interactions is associated with a systematic decrease in the magnitude of nanoparticle-heptane and nanoparticle-toluene interaction energies. The trends of nanoparticles-water and nanoparticles-hydrocarbons energetic interactions as SDS concentrations increase confirm the displacement of nanoparticles from the interfaces toward the aqueous phase by SDS molecules. The displacement of the nanoparticles toward the aqueous phase is also confirmed by the increase of the average number of water molecules in the first coordination shell of the hydroxyl group on the surface of the nanoparticles (see Table 1). The number of Owater in the first coordination shell of OH_{silica} increases systematically with the increase of SDS concentrations in the hydrocarbon phases, indicating the increase of water density around the displaced nanoparticles. The enhanced solvation of silica nanoparticles due to the displacement into the aqueous phase is associated with an increase in the number of the hydrogen bonds between the hydroxyl groups on the surface of the nanoparticles and the surrounding water molecules (see Fig. S4†).

van der Waals interactions contribute significantly to the coexistence of silica nanoparticles and SDS surfactant at the interfaces of water-heptane and water-toluene emulsions, with electrostatic interactions having minor contribution (see Table 2). van der Waals and electrostatic interactions increase systematically with the concentrations of SDS due to the assembly of SDS at the interfaces. Further, van der Waals and electrostatic interactions between the interfacial nanoparticles and surfactants are higher at water-toluene compared to at water-heptane at all SDS concentrations. The higher intermolecular interactions of nanoparticles-SDS at the interface of water-toluene explains the significant reduction in the interfacial tension driven by the synergetic interactions between the interfacial nanoparticles and surfactants. However, the

Table 2 van der Waals and electrostatic interactions (kJ mol⁻¹) of silica nanoparticles with SDS surfactant at the interfaces of water-heptane and water-toluene as a function of SDS concentrations. The data are averaged over the last 10 ns of the simulation time and the error bars represent the standard deviation from the mean value of three different simulations

SDS concentration (wt%)	Water-heptane interface		Water-toluene interface	
	van der Waals	Electrostatic	van der Waals	Electrostatic
0.001	-2.52 ± 0.04	-0.43 ± 0.02	-2.60 ± 0.01	-0.45 ± 0.04
0.01	-16.10 ± 0.12	-2.41 ± 0.08	-23.05 ± 0.27	-3.35 ± 0.09
0.1	-43.25 ± 1.39	-5.19 ± 0.42	-69.207 ± 2.03	-11.02 ± 0.21

Paper

Nanoscale

Table 3 van der Waals and electrostatic interactions of silica nanoparticles with water, heptane and toluene phases (kJ mol $^{-1}$) as a function of SDS concentrations. The data are averaged over the last 10 ns of the simulation time and the error bars represent the standard deviation from the mean value of three different simulations

SDS concentration (wt%)	Silica nanoparticles-water interactions		Silica nanoparticles-hydrocarbon interactions	
	van der Waals	Electrostatic	van der Waals	Electrostatio
Water-heptane				
0	1435.4 ± 11	-18805.4 ± 49	-1150.67 ± 11	-45.46 ± 5
0.001	1461.8 ± 12	$-20\ 155.9 \pm 48$	-874.658 ± 16	-33.65 ± 4
0.01	1489.8 ± 19	-20495.0 ± 31	-748.29 ± 8	-26.18 ± 1
0.1	1499.3 ± 20	-20545.6 ± 19	-634.7 ± 12	-22.14 ± 2
Water-toluene				
0	1378.1 ± 10	-19614.7 ± 53	-884.7 ± 14	-970.2 ± 12
0.001	1454.0 ± 23	$-20\ 135.9 \pm 49$	-774.7 ± 18	-953.4 ± 11
0.01	1476.7 ± 23	$-20\ 224.0\pm51$	-648.3 ± 13	-951.1 ± 13
0.1	1527.3 ± 16	$-21\ 426.6 \pm 21$	-534.7 ± 9	-353.4 ± 6

increase in the hydrogen bonding of nanoparticles-water (Fig. S4†) and SDS-water (Fig. S5†) with the increase of SDS concentrations confirms the favorable adsorption of SDS surfactant at the interface over the silica nanoparticles.

Interestingly, attractive electrostatic interactions of nanoparticles with water are noted while the van der Waals interactions between the OH-terminated nanoparticles and water molecules are repulsive (see Table 3). Hydrogen bonding between the hydroxyl groups on the nanoparticles surfaces and water molecules contributed positively to the strong attraction between the nanoparticles and the aqueous phase. Nanoparticle interactions with heptane are dominated by van der Waals interactions with minor contributions of Coulomb attraction, while the interaction with toluene includes a substantial contribution from van der Waals and electrostatic interactions. The interaction energies elucidate the systematic displacement of silica nanoparticles from water-heptane and water-toluene interfaces that observed from USAXS/SAXS measurements, cryo-SEM imaging and MD simulations.

Conclusions

In this study, we uncover the mechanisms underlying the stabilization of water-toluene and water-heptane emulsions in the presence of silica nanoparticles with diameters of 50 nm and 100 nm and surfactant concentrations ranging from 0.001 wt% to 0.1 wt%. At low SDS concentrations of 0 wt% and 0.001%, emulsion stabilization proceeds via the assembly of silica nanoparticles at water-hydrocarbon interfaces. However, at higher SDS concentrations of 0.1%, emulsion stabilization occurs via the assembly of surfactant at the water-hydrocarbon interfaces and the associated displacement of silica nanoparticles away from these interfaces. The interfacial tensions and the energetics calculated from the simulations underlying these emulsion stabilization mechanisms support experimental observations of the differences in the assembly of silica nanoparticles and SDS surfactant at the water-hydrocarbon interfaces. The reduction in the interfacial tensions

occurs solely due to the assembly of silica nanoparticles at the interfaces in the presence of low SDS concentrations. However, the interfacial tensions reduce significantly in the presence of 0.1% SDS because of the assembly of surfactant that displace the interfacial nanoparticles toward the aqueous phase. These insights provide the physico-chemical basis for designing energy-efficient water and hydrocarbon separations to advance sustainable energy and environmental technologies. Further experimental and computational studies are needed to resolve the effect of the surface curvature of silica nanoparticles and their solutions' pH on their interfacial behavior at immiscible liquids interfaces.

Conflicts of interest

There are no conflicts to declare.

Acknowledgements

This work was supported as part of the Multi-Scale Fluid-Solid Interactions in Architected and Natural Materials (MUSE), an Energy Frontier Research Center funded by the U.S. Department of Energy, Office of Science, Basic Energy Sciences under Award # DE-SC0019285. The use of the Advanced Photon Source, an Office of the Science User Facility operated for the U.S. Department of Energy (DOE) Office of Science by Argonne National Laboratory, is supported by the U.S. DOE under Contract DE-AC02-06CH11357. The authors would also like to acknowledge Dr. Katie Spoth for assisting with the Cryogenic SEM images at Cornell Center for Materials Research shared facilities which is supported through the NSF MRSEC program (DMR-1719875).

References

1 N. Yekeen, E. Padmanabhan, A. K. Idris and S. M. Ibad, J. Pet. Sci. Eng., 2019, 179, 841-854.

- 2 C. Omurlu, H. Pham and Q. P. Nguyen, Appl. Nanosci., 2016, 6, 1167-1173.
- 3 S. Rahman, J. J. Tamborski, M. A. Charette and J. K. Cochran, Mar. Chem., 2019, 208, 29-42.
- 4 J. Faria, M. P. Ruiz and D. E. Resasco, Adv. Synth. Catal., 2010, 352, 2359-2364.
- 5 L. Leclercq, A. Mouret, A. Proust, V. Schmitt, P. Bauduin, J. M. Aubry and V. Nardello-Rataj, Chem. - Eur. J., 2012, 18, 14352-14358.
- 6 F. Tang, L. Li and D. Chen, Adv. Mater., 2012, 24, 1504-
- 7 M. Manzano and M. Vallet-Regí, Adv. Funct. Mater., 2020, 30, 1902634.
- 8 Z. H. Zhou, J. Wang, X. Liu and H. S. O. Chan, J. Mater. Chem., 2001, 11, 1704-1709.
- 9 E. B. Mock, H. De Bruyn, B. S. Hawkett, R. G. Gilbert and C. F. Zukoski, Langmuir, 2006, 22, 4037–4043.
- 10 P. Shinde, S. S. Gupta, B. Singh, V. Polshettiwar and B. L. Prasad, J. Mater. Chem. A, 2017, 5, 14914-14921.
- 11 S. Hasebe, S. Aoyama, M. Tanaka and H. Kawakami, J. Membr. Sci., 2017, 536, 148-155.
- 12 A. Burns, P. Sengupta, T. Zedayko, B. Baird and U. Wiesner, Small, 2006, 2, 723-726.
- 13 M. Lundqvist, I. Sethson and B. H. Jonsson, Langmuir, 2004, 20, 10639-10647.
- 14 S. J. D. Sofla, L. A. James and Y. Zhang, Fuel, 2018, 216,
- 15 E. Dickinson, Trends Food Sci. Technol., 2012, 24, 4-12.
- 16 K. Zhang, Q. Wang, H. Meng, M. Wang, W. Wu and J. Chen, *Particuology*, 2014, **14**, 12–18.
- 17 R. Pichot, F. Spyropoulos and I. T. Norton, J. Colloid Interface Sci., 2012, 377, 396-405.
- 18 T. V. Vu and D. V. Papavassiliou, J. Colloid Interface Sci., 2019, 553, 50-58.
- 19 H. Ma, M. Luo and L. L. Dai, Phys. Chem. Chem. Phys., 2008, 10, 2207-2213.
- 20 N. G. Eskandar, S. Simovic and C. A. Prestidge, Phys. Chem. Chem. Phys., 2007, 9, 6426-6434.
- 21 A. J. Worthen, L. M. Foster, J. Dong, J. A. Bollinger, A. H. Peterman, L. E. Pastora, S. L. Bryant, T. M. Truskett, C. W. Bielawski and K. P. Johnston, Langmuir, 2014, 30, 984-994.
- 22 R. U. Ranatunga, C. T. Nguyen, B. A. Wilson, W. Shinoda and S. O. Nielsen, Soft Matter, 2011, 7, 6942-6952.
- 23 B. P. Binks and J. A. Rodrigues, Langmuir, 2007, 23, 7436-7439.
- 24 I. Akartuna, A. R. Studart, E. Tervoort, U. T. Gonzenbach and L. J. Gauckler, Langmuir, 2008, 24, 7161-7168.
- 25 B. P. Binks and C. P. Whitby, Colloids Surf., A, 2005, 253, 105-115.
- 26 W. Wang, Z. Zhou, K. Nandakumar, Z. Xu and J. H. Masliyah, J. Colloid Interface Sci., 2004, 274, 625–630.
- 27 N. R. Biswal, N. Rangera and J. K. Singh, J. Phys. Chem. B, 2016, 120, 7265-7274.
- 28 R. Pichot, F. Spyropoulos and I. T. Norton, J. Colloid Interface Sci., 2010, 352, 128-135.

- 29 C. Vashisth, C. P. Whitby, D. Fornasiero and J. Ralston, J. Colloid Interface Sci., 2010, 349, 537-543.
- 30 S. Levine, B. D. Bowen and S. J. Partridge, Colloids Surf., 1989, 38, 325-343.
- 31 D. E. Tambe and M. M. Sharma, J. Colloid Interface Sci., 1993, 157, 244-253.
- 32 J. H. Schulman and J. Leja, Trans. Faraday Soc., 1954, 50, 598-605.
- 33 E. H. Lucassen-Reynders and M. V. D. Tempel, J. Phys. Chem., 1963, 67, 731-734.
- 34 H. Hassander, B. Johansson and B. Törnell, Colloids Surf., 1989, 40, 93-105.
- 35 F. Ravera, E. Santini, G. Loglio, M. Ferrari and L. Liggieri, I. Phys. Chem. B, 2006, 110, 19543-19551.
- 36 J. Wang, F. Yang, C. Li, S. Liu and D. Sun, Langmuir, 2008, 24, 10054-10061.
- 37 S. Mohammed, H. Asgar, I. Kuzmenko and G. Gadikota, Energy Fuels, 2020, 34, 12545-12555.
- 38 J. Ilavsky, P. R. Jemian, A. J. Allen, F. Zhang, L. E. Levine and G. G. Long, J. Appl. Crystallogr., 2009, 42, 469-479.
- 39 J. Ilavsky, F. Zhang, A. J. Allen, L. E. Levine, P. R. Jemian and G. G. Long, Metall. Mater. Trans. A, 2013, 44, 68-76.
- 40 J. Ilavsky, J. Appl. Crystallogr., 2012, 45, 324-328.
- 41 J. Ilavsky and P. R. Jemian, J. Appl. Crystallogr., 2009, 42, 347-353.
- 42 G. Yu and J. Zhou, Phys. Chem. Chem. Phys., 2016, 18, 23500-23507.
- 43 D. Argyris, N. R. Tummala, A. Striolo and D. R. Cole, J. Phys. Chem. C, 2008, 112, 13587-13599.
- 44 D. Argyris, D. R. Cole and A. Striolo, Langmuir, 2009, 25, 8025-8035.
- 45 A. Phan, D. R. Cole and A. Striolo, J. Phys. Chem. C, 2014, 118, 4860-4868.
- 46 R. T. Cygan, J. J. Liang and A. G. Kalinichev, J. Phys. Chem. B, 2004, **108**, 1255–1266.
- 47 W. L. Jorgensen, J. D. Madura and C. J. Swenson, J. Am. Chem. Soc., 1984, 106, 6638-6646.
- 48 W. L. Jorgensen, D. S. Maxwell and J. Tirado-Rives, J. Am. Chem. Soc., 1996, 118, 11225-11236.
- 49 V. S. Farafonov and A. V. Lebed, J. Chem. Theory Comput., 2017, 13, 2742-2750.
- 50 T. Fang, Y. Zhang, R. Ma, Y. Yan, C. Dai and J. Zhang, Appl. Surf. Sci., 2019, 494, 80-86.
- 51 B. Meghwal, N. Rampal and A. Malani, Energy Fuels, 2020, 34, 16023-16034.
- 52 H. Yan and S. Yuan, J. Phys. Chem. C, 2016, 120, 2667-
- 53 S. Nosé, Mol. Phys., 1984, 52, 255-268.
- 54 W. G. Hoover, Phys. Rev. A, 1985, 31, 1695.
- 55 M. Parrinello and A. Rahman, J. Chem. Phys., 1982, 76, 2662-2666.
- 56 T. Darden, D. York and L. Pedersen, J. Chem. Phys., 1993, 98, 10089-10092.
- 57 M. J. Abraham, T. Murtola, R. Schulz, S. Páll, J. C. Smith, B. Hess and E. Lindahl, *SoftwareX*, 2015, 1, 19–25.

Nanoscale Paper

- 58 Y. Chai, J. Hasnain, K. Bahl, M. Wong, D. Li, P. Geissler, P. Y. Kim, Y. Jiang, P. Gu, S. Li and D. Lei, *Sci. Adv.*, 2020, **6**, eabb8675.
- 59 M. Zargartalebi, N. Barati and R. Kharrat, *J. Pet. Sci. Eng.*, 2014, **119**, 36–43.
- 60 T. Li, A. J. Senesi and B. Lee, *Chem. Rev.*, 2016, **116**, 11128–11180.
- 61 A. Czajka and S. P. Armes, *J. Am. Chem. Soc.*, 2021, **143**, 1474–1484.
- 62 S. Svenson, Curr. Opin. Colloid Interface Sci., 2004, 9, 201–212.
- 63 W. Shinoda, R. DeVane and M. L. Klein, *Soft Matter*, 2008, 4, 2454–2462.
- 64 W. X. Shi and H. X. Guo, J. Phys. Chem. B, 2010, 114, 6365-6376.

- 65 P. W. Schmidt, J. Appl. Crystallogr., 1991, 24, 414-435.
- 66 J. Teixeira, J. Appl. Crystallogr., 1988, 21, 781-785.
- 67 T. Lan, H. Zeng and T. Tang, J. Phys. Chem. C, 2019, 123, 22989–22999.
- 68 X. Sun, H. Zeng and T. Tang, J. Colloid Interface Sci., 2021, 586, 766–777.
- 69 S. Mohammed and G. A. Mansoori, *Energy Fuels*, 2018, 32, 5409–5417.
- 70 S. Mohammed and G. A. Mansoori, *J. Mol. Liq.*, 2018, **263**, 268–273.
- 71 A. H. S. Dehaghani, M. S. Taleghani, M. H. Badizad and R. Daneshfar, *Colloid Interface Sci. Commun.*, 2019, 33, 100202.